Microstructure and mechanical properties after thermal treatments of biomedical Ti-6Al-4V alloy produced by laser sintering

P. Mengucci[1]*, G. Barucca[1], A. Gatto[2], E. Bassoli[2], L. Denti[2], F. Fiori[3], E. Girardin[3], P. Bastianoni[1], B. Rutkowski[4], A. Czyrska-Filemonowicz[4]

[1] Dipartimento SIMAU, Università Politecnica delle Marche, 60131 Ancona, Italy.

[2] Dipartimento DIEF, Università di Modena e Reggio Emilia, Via Vivarelli 10, 41125 Modena, Italy.

[3] Dipartimento DISCO, Università Politecnica delle Marche, 60131 Ancona, Italy.

[4] International Centre of Electron Microscopy for Material Science & Faculty of Metals Engineering and Industrial Computer Science, AGH University of Science and Technology, Al. A. Mickiewicza 30, 30-059 Kraków, Poland.

*** Corresponding author:**

Paolo Mengucci
Dip. SIMAU, Università Politecnica delle Marche
I-60131 Ancona
Italy
E-mail: p.mengucci@univpm.it

Abstract

Keywords: Ti alloys; laser sintering; heat treatments; mechanical properties; structure characterization.

1. Introduction

2. Material and methods

2.1 Sintering parameters, material composition and properties

Starting from EOS Ti64 powder, supplied by EOS GmbH Electro Optical System, flexural and tensile specimens were produced by Direct Metal Laser Sintering (DMLS). An EOSINT M270 system equipped with a solid-state Yb fiber laser carried out the sintering process by using the laser sintering parameters reported in Table 1.

Table 1 Sintering parameters used for DMLS.

Laser power	200 W
Laser spot diameter	200 μm
Scan speed	up to 7.0 m/s
Building speed	2 - 20 mm^3/s
Layer thickness	20 μm
Protective atmosphere	Oxygen (max 1.5%)

The material is Ti-6Al-4V alloy with chemical composition corresponding to ISO 5832-3, ASTM F1472 and ASTM B348. Nominal composition of the EOS Ti64 powder, as reported in the material datasheet provided by the manufacturer, is shown in Table 2.

Table 2 Nominal composition of EOS Ti64 powder.

Al	V	O	N	C	H	Fe	Ti

(wt.%)	(wt.%)	(ppm)	(ppm)	(ppm)	(ppm)	(ppm)	
5.50 - 6.75	3.50 - 4.50	< 2000	< 500	< 800	< 150	< 3000	Balance

Material properties from the producer datasheet are listed in Table 3 for the as-sintered (AS) and heat-treated (HT) conditions. Heat treatment, performed soon after the laser production process in order to reduce anisotropies due to the layer-by-layer building method, consists of thermal heating the AS sample at 800 °C for 4 hours in argon inert atmosphere. From now on, this thermal treatment is referred to as HT.

Mechanical properties in Table 3 are expressed as minimum values to indicate that they exceed the minimum requirements of material specification standards ASTM F1472-08, ASTM B348-09 and ISO 5832-3:2000.

Table 3 Material properties as reported in the material datasheet for the as sintered (AS) material and after thermal treating at 800 °C for 4 hours in argon atmosphere (HT).

	AS	**HT**
Density [g/cm^3]	4.41	
UTS [MPa]	1230 ± 50	1050 ± 20
$R_{p0.2}$ [MPa]	1060 ±50	1000 ± 20
Elongation at break [%]	10 ± 2	14 ± 1
Young's Modulus [GPa]	110 ± 10	116 ± 10
Hardness (HRC)	41-44	

It is evident from Table 3 that metal parts in the HT state shows a decrease of about 15% in strength and an increase of about 40% in elongation values with respect to the AS condition, while Young

modulus and hardness remain unaltered. These variations in UTS and elongation values are due to the HT treatment performed soon after the production process.

It is worth to note that all metal parts produced by EOS GmbH in Ti64 alloy for biomedical applications are commercialized in the HT state. Therefore, the HT state is the reference state of the samples investigated in this study and the values reported in Table 3 for the HT state are the reference values for the mechanical properties of our samples.

2.2 Mechanical tests and firing cycle

Flexural specimens (FLEX) were produced according to ASTM B528-05 (Standard Test Method for Transverse Rupture Strength of Metal Powder Specimens) and B 925–08 (Standard Practices for Production and Preparation of Powder Metallurgy (PM) Test Specimens).

Tensile specimens (TENS) were built following ASTM E8M:11 (Standard Test Methods for Tension Testing of Metallic Materials).

Figure 1 shows geometry and dimensions of FLEX (Fig. 1a) and TENS (Fig. 1b) samples, respectively. In both drawings, Z is the direction of growth in the AM machine, and XY is the plane of powder deposition; X is the slide direction of the recoater. Dimensions in Figure 1 are in mm.

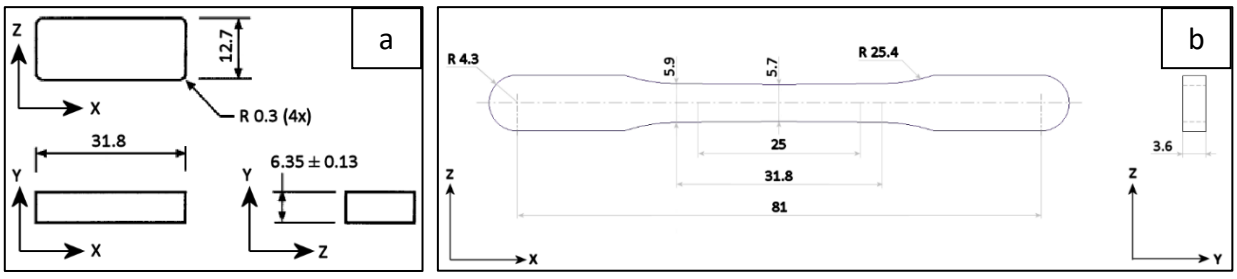

Figure 1 Geometry of samples produced for mechanical tests: a) flexural (FLEX), b) tensile (TENS_0). Dimensions in mm.

In order to investigate possible variations of the mechanical properties with the sample building orientation, three different groups of tensile (TENS) specimens were produced. Each group consisted of 4 tensile samples. The different groups of samples were built with the axis of the tensile specimens oriented along three different directions of the building machine, as follows:

- TENS_0: axis parallel to the X direction;
- TENS_90: axis parallel to the Y direction;
- TENS_45: axis parallel to the bisector of the X-Y quadrant.

After additive fabrication, all samples belonging to both TENS and FLEX groups were submitted to the HT treatment. As already stated above, this represents the reference condition of our samples, which simulates the normal condition of commercialization of metallic devices obtained by additive manufacturing.

However, in dental applications, due to aesthetic reasons, metallic devices are often veneered with dental ceramic material during a firing operation carried out at high temperature. This further thermal treatment, can induce modifications of microstructure and consequently of mechanical properties of the metallic devices. Therefore, in order to investigate also possible variations of mechanical properties and microstructure of the Ti-6Al-4V alloy due to the firing cycle (FC), a five-step thermal treatment was adopted in this work. Details of this standard five-step cycle, compliant to EN ISO 22674, are outlined in Figure 2. Starting from a pre-heating temperature of 420 °C, five steps simulate the firing of oxide and ceramic layers.

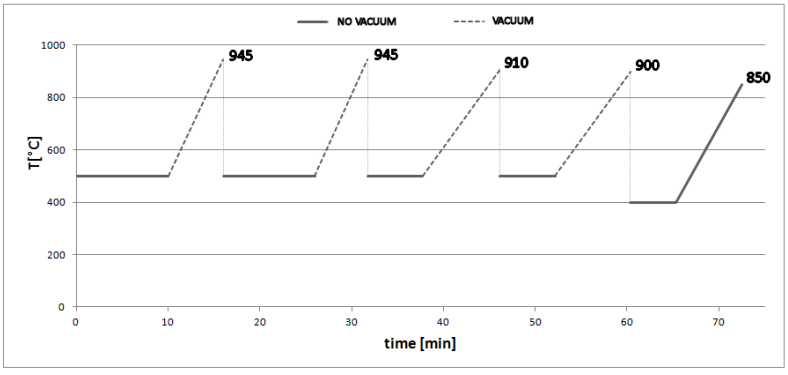

Figure 2 Thermal cycle used for fire simulation. The cooling phase between each firing step is not represented.

In total, four samples of the FLEX group were submitted to the firing cycle (Fc) described above. From now on, samples belonging to this thermally treated group are indicated as $FLEX_{FC}$.

Details of the mechanical tests performed on samples of the TENS, FLEX and $FLEX_{FC}$ groups are summarized in the following:

- Tensile tests (crosshead speed 5 mm/min, load cell capacity 250 kN);
- Three point bending tests (support width 25.4 mm, crosshead speed 2 mm/min, load cell capacity 30 kN).

2.3 Hardness measurements

Rockwell C hardness tests, based on ISO 4498:2010 (Sintered metal materials, excluding hard metals -- Determination of apparent hardness and microhardness), were performed by means of an ERNST NR3D Hardness tester, following the specifications of ISO 6508-1:2015 (Metallic materials -- Rockwell hardness test).

2.4 Roughness measurements

Roughness measurements adhering to EN 10049:2013 were carried out by means of a DIAVITE DH-5 stylus tester, by adopting a travel length l_t of 4.8 mm, with a cut-off filter of 0.8 mm, giving an evaluation length l_m of 4 mm. Five measurements per sample were recorded for statistical reasons, taken on XZ faces along the X direction. The standard deviations (SD) associated to the roughness value were estimated from the five measurements.

2.5 Statistical tests

Statistical tests were performed in order to assess whether the heat treatments cause significant changes in the mechanical response. Possible significant differences between the groups were checked by means of the t-test for independent samples by using a software tool for statistical analysis (Statistica 8, Statsoft). The test can be used to determine if two sets of data are significantly different from each other. It results in probability values (p-values): when lower than 0.05 they can be taken as a decision to reject the null hypothesis of equality between two groups of samples.

2.6 Structure characterization

In order to correlate the mechanical behavior of samples to their microstructure, samples from the TENS, FLEX and $FLEX_{FC}$ groups were structurally characterized by the analytical techniques listed below. All samples submitted to structural characterization were not mechanically tested. Morphological and structural characterization of the EOS-Ti64 powder was also performed.

Structural characterizations were carried out by X-ray diffraction (XRD), scanning electron microscopy (SEM), transmission electron microscopy (TEM), scanning transmission electron microscopy (STEM) and energy dispersive X-ray microanalysis (EDX).

A Bruker D8 Advance diffractometer operating at V= 40kV and I= 40 mA, with Cu-Kα radiation, in the angular range 2θ=10 - 80° was used for XRD measurements.

SEM observations were carried out by a Zeiss Supra 40 field emission scanning electron microscope (FE-SEM) equipped with a Bruker Z200 EDX microanalysis.

A Philips CM200 and a JEOL JEM-2010 ARP equipped with an Oxford Inca energy dispersive X-ray microanalysis, both operating at 200 kV, were used for TEM observations and EDX analysis.

Analytical high resolution microscopy was carried out by a probe Cs-corrected FEI Titan^3 G2 60-300 equipped with ChemiSTEM technology (X-FEG field-emission gun and Super-X EDX detector system) developed at FEI (FEI application note AN002707-2010. Available from: www.fei.com).

TEM bright-field imaging and STEM imaging using high-angle annular-dark-field (HAADF) contrast as well as EDX mapping and high-resolution TEM (HRTEM) imaging were used for

characterization of the samples micro/nanostructure and chemical composition of phases down to the nano-scale. Phase identification was performed by selected area electron diffraction (SAED), STEM-EDX and fast Fourier transform (FFT) of HRTEM images. The diffraction patterns and HRTEM images were interpreted with the JEMS software (Stadelman 2007).

Samples for TEM observations were mechanically prepared by grinding on abrasive papers and diamond pastes. Disks with a 3 mm diameter were cut from the bulk material by an ultrasonic cutter (Gatan). In order to reduce time of ion milling, in the last step of the mechanical thinning procedure, each 3 mm disk was mechanically thinned in a central area by a Dimple Grinder (Gatan). Final thinning was carried out by an ion beam system (Gatan PIPS) using Ar ions at 5 kV.

Samples (lamellae) for STEM, HRTEM and EDX analyses were prepared by Focused Ion Beam (FIB) technique by the ZEISS NEON CrossBeam 40EsB microscope. Before milling, a layer of Pt was deposited at the place of cutting in order to protect the thin sample against heavy Ga ions during the preparation. Final milling was performed with the 4 keV Ga+ beam.

3. Results

3.1 Roughness measurements

Roughness measurements provided values in the same range for all the specimens. The average value of the average roughness R_a was 6.69 μm, with a standard deviation (SD) of 1.83 μm. As to maximum roughness R_{max}, an average value of 44.62 μm (SD = 18.78 μm) was obtained.

3.2 Hardness and mechanical tests

Results of tensile and hardness tests on tensile specimens (TENS) are shown in table 4, separately for the different groups of samples (TENS_0, TENS_45, TENS_90). The average value (AV) is reported with the corresponding standard deviation (SD). All samples prove to have a HRC value around 40 independently on the axis orientation during production. Elongation at break is around 12% for all samples while a slight decrease in UTS is found between TENS_0 and TENS_90.

Table 4 Average value (AV) and standard deviation (SD) of ultimate tensile strength (UTS), strain at break (ε_b) and Rockwell C hardness (HRC) of the tensile specimens (TENS).

	UTS (MPa)		ε_b (%)		HRC	
	AV	SD	AV	SD	AV	SD
TENS_0	1110	1	12	2	39.8	2.6
TENS_45	1098	26	13	1	38.7	3.9
TENS_90	1080	6	11	1	38.9	2.5

Results for flexural properties are listed in Table 5, separately for the untreated samples (FLEX) and for those that underwent the firing cycle ($FLEX_{FC}$). Average value (AV) and standard deviation (SD) as obtained from the experimental investigations are listed in Table 5 for hardness (HRC) and transverse rupture strength (TRS). In this case, results in Table 5 evidences a reduction of both hardness and strength of the flexural samples after the firing cycle.

Table 5 Average value (AV) and standard deviation (SD) of Rockwell C hardness (HRC) and transverse rupture strength (TRS) of the flexural specimens.

	HRC		TRS (MPa)	
	AV	SD	AV	SD
FLEX	44.9	0.6	2566	39.3
$FLEX_{FC}$	40.7	2.7	2359	28.7

Results of statistical tests relating mechanical properties of TENS and FLEX groups of samples are reported in Table 6 in terms of p-value, estimated by statistical analysis software tool. Table 6 confirms the statistical significance of the mechanical properties variations evidenced above.

Table 6 p-values resulting from the t-test for the variables UTS, ε_b, HRC and TRS among the different groups of samples. Records below the level of significance of 0.05 are underlined.

	p-values			
	UTS (MPa)	ε_b (%)	HRC	TRS
TENS_0 - TENS_45	0.36	0.36	0.29	-
TENS_0 - TENS_90	0.00	0.70	0.26	-
TENS_45 - TENS_90	0.30	0.14	0.86	-
$FLEX_{FC}$ -FLEX	-	-	0.00	0.00

3.3 Morphological and chemical characterization (FE-SEM, EDX)

Morphology and size distribution of particles in the EOS Ti64 powder are shown in Figure 3. The FE-SEM image in Figure 3a shows morphology and size of spherical particles in the Ti64 starting powder, while the histogram in Figure 3b reports the distribution of particles diameter.

Quantitative analysis of SEM images were carried out by ImageJ software (version 1.50b) [ref] while statistical information on particles size were obtained by Origin [ref]. Particles diameter ranges from 0.7 μm to 118 μm with an average size of 16 μm, as estimated from the image in Figure 3a.

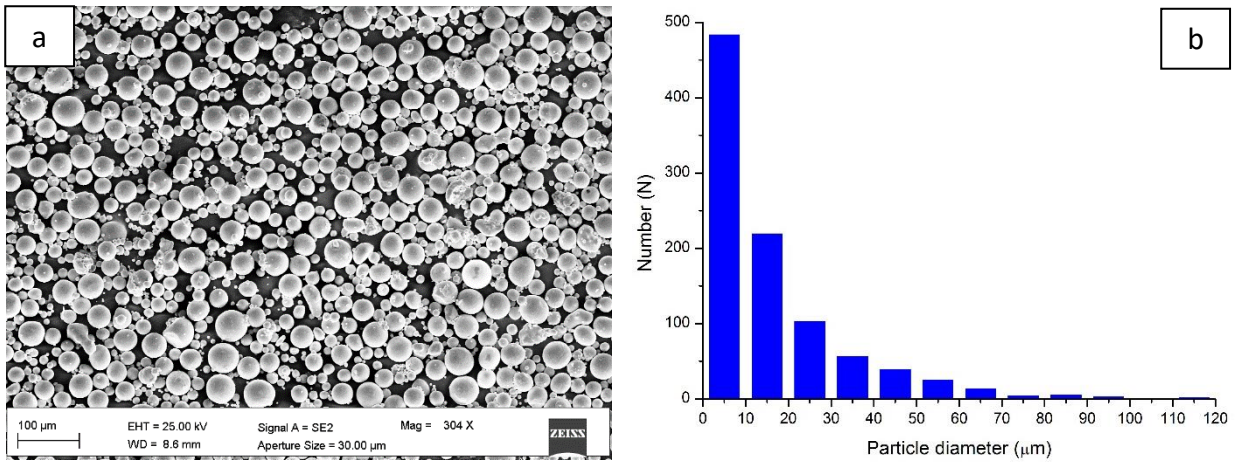

Figure 3 EOS Ti64 powder: a) field emission SEM image, b) size distribution of particle diameter.

Chemical characterization of samples was carried out by EDX analysis performed during the FE-SEM observations. At least, five different large areas at same magnification (~300 x) for each sample were investigated. EDX analysis performed on powder (PW), on samples in the reference condition (FLEX) and after the firing cycle ($FLEX_{FC}$) provided the results shown in Table 7. It is worth to note, that for all samples the Al content is within the nominal range while the V content is always lower than expected, even in the powder.

Table 7 Element concentration (in wt%) obtained from SEM-EDX analysis of powder and samples in the reference condition (FLEX) and after the firing cycle ($FLEX_{FC}$).

Sample	Al	V	Ti
Powder	6±1	3.3±0.3	91±7
FLEX	6±1	2.5±0.3	92±7
$FLEX_{FC}$	6±1	2.5±0.3	91±7

3.4 Crystallographic characterization (XRD)

The crystallographic structure of samples was investigated by XRD. Results for powder and samples in the reference condition (FLEX) and after the firing cycle ($FLEX_{FC}$) are shown in Figure 4. At least two samples for each condition from the different groups were measured.

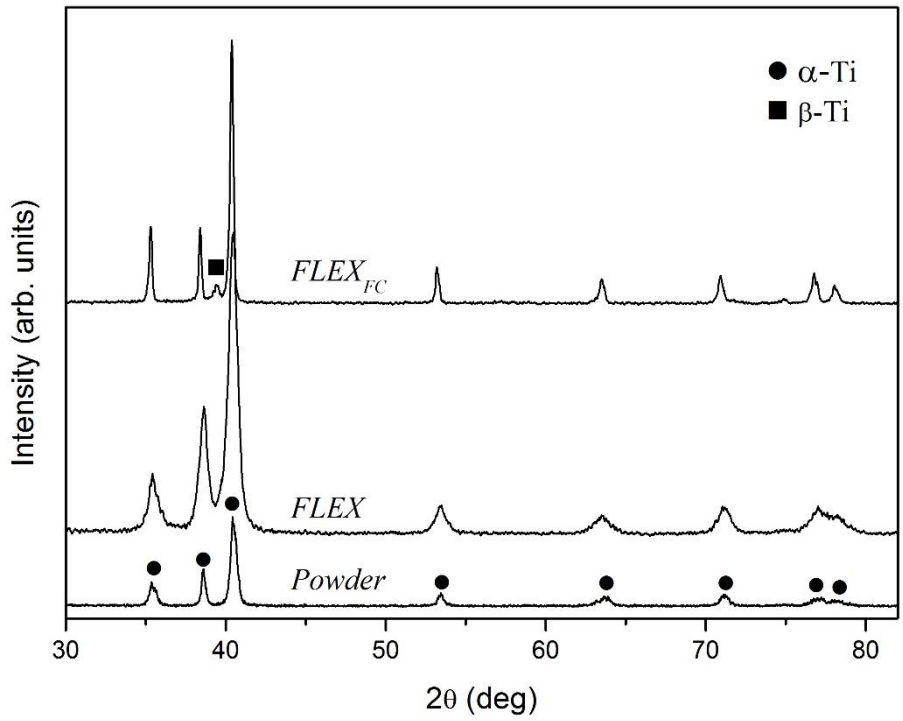

Figure 4 XRD patterns of powder, sample in the reference condition (FLEX) and after the firing cycle ($FLEX_{FC}$).

Rietveld analysis of the XRD patterns, performed by the Maud program [ref], allowed estimating the lattice parameters of phases present in each sample. Results of peak analysis are reported in Table 8 with experimental error provided by the Maud software. Last raw in Table 8 reports the nominal lattice parameters from the International Centre for Diffraction Data (ICDD) of α-Ti (card n. 44-1294) and β-Ti (card n. 44-1288), respectively.

Table 8 Experimental lattice parameters calculated from peak position in the XRD patterns. Last raw reports the nominal lattice parameter values from cards of the International Centre for Diffraction Data (ICDD).

Sample	**α-Ti (nm)**	**β-Ti (nm)**
Powder	a = 0.2922 ± 0.0001 c = 0.4659 ± 0.0001	-
FLEX	a = 0.2922 ± 0.0002 c = 0.4658 ± 0.0004	-
$FLEX_{FC}$	a = 0.2930 ± 0.0001 c = 0.4681 ± 0.0003	a = 0.323 ± 0.002
Nominal	a = 0.29505 c = 0.46826 ICDD card n. 44-1294	a = 0.33065 ICDD card n. 44-1288

Powder composition is 100% hexagonal (hcp) low temperature α-Ti phase. Same composition (100% hcp α-Ti) is found in the FLEX sample. Only after the firing cycle ($FLEX_{FC}$) a small peak at 2θ=39.46° (full square in Figure 4) attributable to the cubic (bcc) high temperature β-Ti phase is present in addition to the α-Ti diffraction peaks. The lattice parameters calculated from the experimental XRD patterns should be compared to nominal values in the ICDD cards, shown in the last raw of Table 8.

Rietveld analysis performed on the XRD pattern of the $FLEX_{FC}$ sample provided a β-Ti phase volume content of about 10%.

3.5 Transmission electron microscopy (TEM, HRTEM, STEM) and microanalysis (EDX)

Figure 5 shows results of TEM observations performed on FLEX (figure 5a) and $FLEX_{FC}$ (figure 5b) samples.

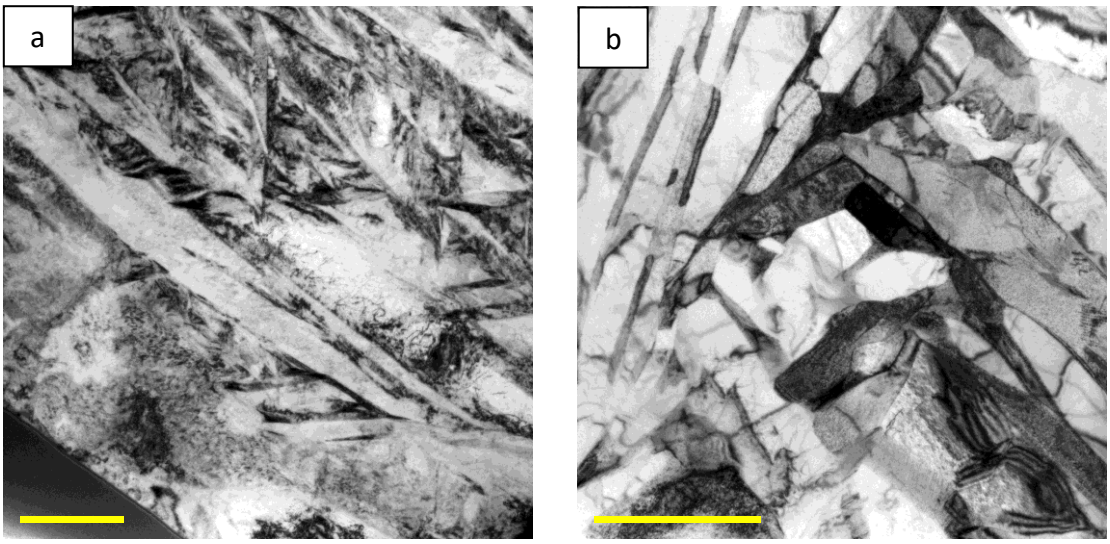

Figure 5 TEM bright field images: a) flexural sample in the reference condition (FLEX) and b) after the firing cycle ($FLEX_{FC}$).

The FLEX sample (figure 5a) shows an acicular microstructure with a high density of dislocations inside the lamellar grains and rare twins.

In the $FLEX_{FC}$ sample (figure 5b) rare equiaxed grain with size up to 1 μm are present although the lamellar morphology of martensitic plates is generally retained. Independently on the grain shape, the dislocation density in the $FLEX_{FC}$ sample is always heavily lower than in the FLEX sample. A further difference between samples in figure 5 is the presence of β-Ti phase at the martensite plate boundaries of the $FLEX_{FC}$ sample (figure 5b). The β-Ti phase forms as elongated layers at the plate boundaries, with variable length up to 2 μm and width up to 100 nm (figure 5b). It is worth to note that the β-Ti layers at plate boundaries do not form a continuous net around the martensitic plates (figure 5b). HRTEM observations performed at plate boundaries allowed studying the crystallographic relationships between martensitic α'-Ti and β-Ti phases, confirming the Burgers relationships [ref].

Information about elements content and distribution inside martensite and β phase were obtained by STEM observations and EDX microanalysis. For the FLEX sample, where the β phase is absent, results showed a uniform distribution of Al and V inside the entire specimen and EDX analysis provided the elements concentration reported in Table 9. On the contrary, for the $FLEX_{FC}$ sample, STEM observations performed in high angle annular dark field (HAADF) mode and EDX elemental mapping showed segregation of V at the plate boundaries in correspondence of the β phase. Figure 6 reports results of STEM investigations and EDX mapping performed with signals from Ti, V and Al. The STEM-HAADF image (figure 6a) evidences compositional contrast preferentially located at the plate boundaries. In particular, well-defined lighter zones not continuously connected are visible at the plate boundaries in figure 6a. The EDX elemental map obtained with signals from Ti, V and Al, performed on the same area of the sample, shows high V concentration in correspondence of the lighter zones (figure 6b). HRTEM observations and selected area electron diffraction (SAED) investigations showed that the V enriched zones are fully composed of β phase.

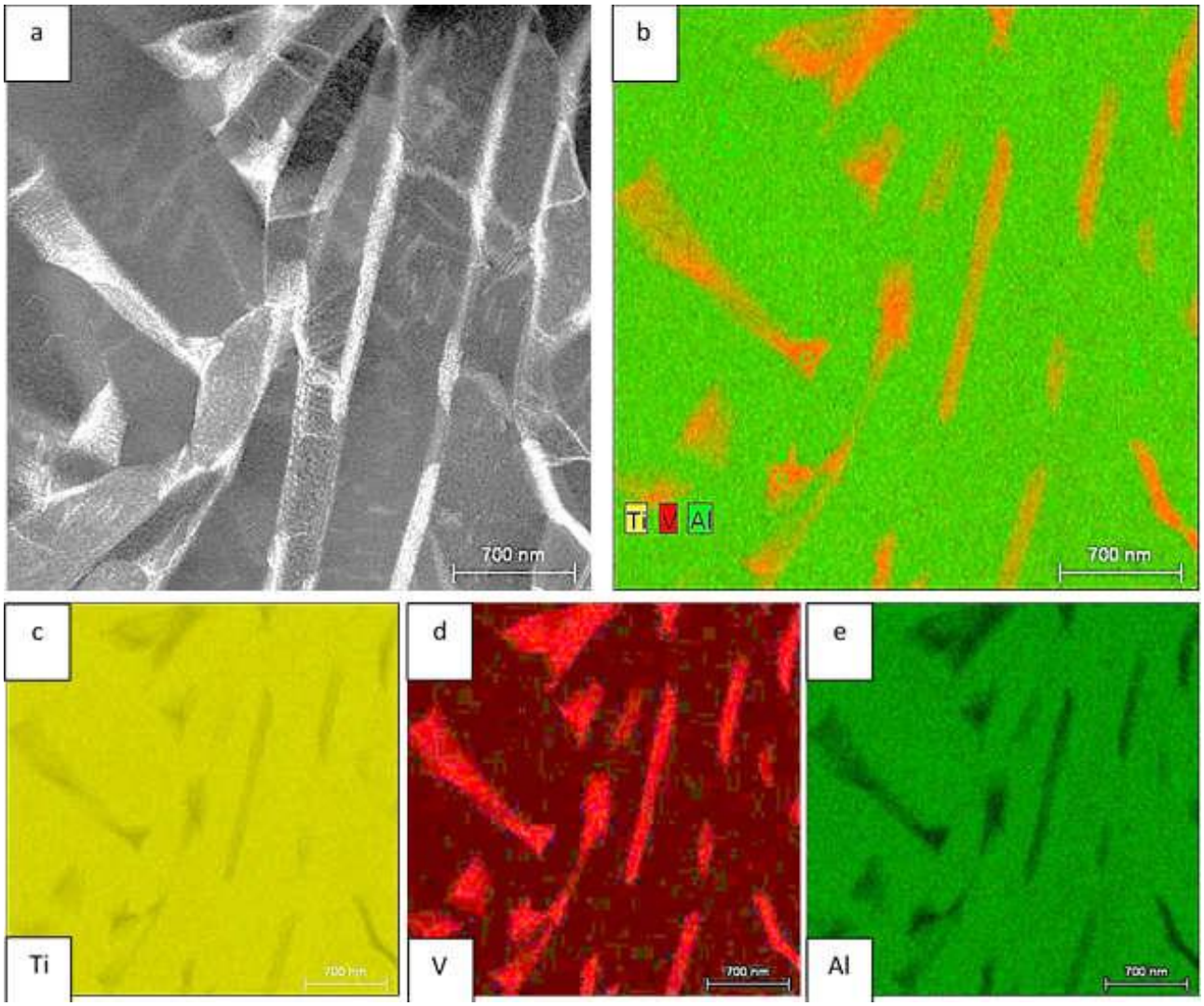

Figure 6 STEM-HAADF image of the $FLEX_{FC}$ sample and corresponding elemental mapping performed with signals from Ti, V and Al: a) HAADF image, b) EDX map obtained by combining signals from Ti, V and Al, c) EDX map of Ti, d) EDX map of V and e) EDX map of Al. (Color references in the web version of the paper).

Distribution of single elements in the same zone of the $FLEX_{FC}$ sample is reported in figures 6c-6e, for Ti, V and Al, respectively. In figures 6c-6e, lighter regions of the image are enriched with the corresponding element used for mapping.

EDX analysis performed in spot mode during the STEM observations allowed estimating the local concentration of elements in different zones of samples. Results obtained for FLEX and $FLEX_{FC}$

samples are shown in Table 9 where for the $FLEX_{FC}$ sample are reported results for both α and β phases. At least five measurements were performed on each Ti phase present in the sample, and the element concentration in Table 9 is expressed as the average value with corresponding standard deviation.

Table 9 Average value and standard deviation from five measurements of element concentration in α-Ti and β-Ti phases obtained by STEM-EDX analysis performed in spot mode on both FLEX and $FLEX_{FC}$ samples. All values are in wt%.

Sample	Ti phase	Al	V	Ti
FLEX	α	6.10±0.03	2.786±0.001	91.12±0.16
$FLEX_{FC}$	α	6.49±0.04	1.95±0.24	91.6±0.3
$FLEX_{FC}$	β	2.77±0.18	20.3±0.5	76.95±0.24

It is worth to note the high concentration of V in the β phase suggesting element partitioning during the α → β transformation induced by firing cycle.

4. Discussion

The Ti alloy considered in this study is the well-known Ti-6Al-4V alloy commonly used in industrial applications, and specifically developed by EOS GmbH Electro Optical System for biomedical applications. Nominal composition of the alloy, provided by the manufacturer, is within the standard compositional range with low content of Fe, H and C (Table 2).

The laser sintering process carried out by using the parameters reported in Table 1 allowed producing tensile (TENS) and flexural (FLEX) samples for the mechanical tests and the structural characterization. After production and thermal treatment at 800 °C for 4 hours (HT), all samples are compact without any visible porosity, with an average surface roughness R_a=6.69 μm. Average surface roughness around the same value was measured also for the $FLEX_{FC}$ group of samples.

Mechanical tests performed on the TENS samples produced in different building orientation show average values of UTS in the range 1080-1110 MPa, with elongations of about 12% (Table 4). All groups proved to have good test repeatability with a very low standard deviation. Regarding tensile strength, although the span among results for different orientations is only 30 MPa, yet the t-test proves the statistical significance of the difference between the groups TENS_0 and TENS_90 (Table 6). On the contrary, no significant effect of build orientation is observed on ductility (Table 4). If compared the nominal values stated by the producer, strength is well above expectations, while elongation at break is slightly lower (Table 3).

Effects of build orientation on the mechanical properties of Ti-6Al-4V alloy are reported for both laser sintering [D1] and electron beam melting [D2] technologies. Inhomogeneity occurs for the high thermal gradients developed during the production process that could induce crystallographic textures capable of influencing the mechanical behavior of the material along specific orientations [D3].

Post-production processes consisting of mechanical and/or thermal treatments are commonly used to reduce effects of build orientation [D1, D2]. However, in most cases, such post-production treatments induce variation of microstructure and consequently of mechanical properties [D3-D5]. In our case, results in Table 4 show that the HT treatment carried out soon after production is not sufficient to remove the structural inhomogeneity causing UTS reduction in the TENS_90 sample. However, the residual inhomogeneity in the TENS_90 sample does not produce any effect on the elongation behavior of the alloy (Table 4 and Table 6).

The experimental values of UTS and elongation obtained in this study (Table 4) are within the range reported in literature for both conventional and additive production technologies [D6-D9] and are even comparable to the values obtained by Xu et al. [D10] after in situ martensite decomposition that produces an ultrafine lamellar ($\alpha+\beta$) structure.

Flexural samples exhibit excellent mechanical properties too, even after the firing cycle that reduces both hardness and strength. In fact, as shown in Table 5 flexural strength in the untreated condition

is as high as 2566 MPa, and decreases to 2359 MPa because of the firing operation. At the same time, hardness goes from 45 to 40 HRC. Both variations are statistically significant, as shown in Table 6.

In terms of microstructure, whose modification produce variation in the mechanical response, the FLEX sample shows the typical α' acicular microstructure of metal parts subject to high cooling rates [D6, D8], with a high density of dislocations inside the lamellar grains and rare twins (Figure 5a). The FLEX sample if completely formed of α' phase with an hcp crystallographic structure and lattice parameters identical to the Ti64 powder (Table 8), even though the average content of V is slightly lower (2.5 wt%) with respect to the powder (3.3 wt%), as shown in Table 7. This latter result is further confirmed by STEM-EDX analysis performed in spot mode reported in Table 9, that shows values of element content in complete agreement with those obtained by SEM-EDX on large areas of the sample (Table 7). Probably, a small amount (<1 wt%) of V is lost during the laser melting process, but this is not enough to cause modifications of the crystallographic lattice parameters (Table 8). Furthermore, from the experimental results in Table 8 it is evident that the crystallographic cell of the hcp α' phase, in powder and FLEX sample, is smaller than the crystallographic cell of the nominal hcp α-Ti phase reported in the ICDD card (Table 8).

After the firing cycle, microstructure and mechanical behavior of the alloy strongly change. Hardness and strength decrease of about 9% and 8%, respectively (Table 5). In terms of microstructure, although the average composition (Table 7) of the sample ($FLEX_{FC}$) is unaltered with respect to the untreated condition (FLEX), XRD investigations show the presence of the bcc β phase in addition to the hcp α' phase (Figure 4). TEM observations show β phase located at the plate boundaries of α' grains (Figure 5b) and confirm the Burgers orientation relationships between the two phases. The volum e fraction of the β phase (about 10%) estimated by Rietveld analysis of XRD pattern was confirmed by STEM-HAADF observations. Attallah et al. [D11] have already demonstrated that combination of XRD and electron microscopy techniques for the estimation of the α/β phase fraction in α+β Ti alloys is a very reliable method.

Calculation of lattice parameters from the XRD pattern (Figure 4) shows an increase of the hcp α' lattice parameters (Table 8) in the treated sample ($FLEX_{FC}$) with respect to the untreated one (FLEX). In particular, the lattice parameter a increases of about 0.3% while c of about 0.5% (Table 8). On the contrary, measured value of the bcc β phase lattice parameter is a=0.323±0.002 nm, about 2% lower than the nominal value reported in the ICDD card (Table 8).

Modification of mechanical behavior in Ti-Al-V alloys as a consequence of shape and crystallography of the constituent phases has been already observed [D12, D13]. In particular, Matsumoto et al. [D13] ascribed the excellent ductility of their Ti-6Al-4V alloy to: a) the single phase hcp (α, α') constituent, b) the fine equiaxed morphology, c) the enrichment of V content and the decrease in Al content of α' martensitic regions during solution treatment.

In our case, the lamellar structure of the α' phase is substantially retained after the firing cycle while the volume fraction of the β phase (about 10%) is limited, therefore the strength reduction observed in our alloy can be only partially attributed to the phase type and morphology in the treated sample.

On the other hand, STEM-HAADF observations and STEM-EDX analysis evidenced a strong partitioning of elements between the β phase at the plate boundaries and the α' plates (Figure 6). Results in Table 9 for the $FLEX_{FC}$ sample clearly show an enrichment of V in the β phase and a slight increase of Al in the α' phase. It is worth to note the high concentration of V (about 20 wt%) and the reduced content of Al (about 3 wt%) in the β phase, as well as the low V content (<2 wt%) in α' phase (Table 9). These results suggest a diffusion controlled mechanism responsible of β formation at the grain boundaries (Figure 6).

Diffusion processes responsible of the α ↔ β transformations in Ti-6Al-4V alloy are already reported in literature [D14-D15]. In (α+β) systems, it was shown that since the diffusivity of V in β is lower than in α, diffusion of V in α produces first an enrichment of the α grain boundaries to which follows a gradual diffusion of V atoms into β [D14]. On the other hand, Barriobero-Vila et al. [D15], in (α+β) systems, supposed the contemporary diffusion of V into β and Ti into α to justify the observed variations of lattice parameters of the two phases. Thermodynamic calculation demonstrated that also

diffusion of Al from α into β can occur during the α → β transformation [D16]. Furthermore, close relationship between variation of lattice parameters and diffusion mechanisms in α and β phases as well as lattice strain relaxation have been reported [D17-D20].

Therefore, the experimental results obtained in the current work indicate that, during the firing cycle, atoms of V diffuse inside the α' phase and accumulate at the plate boundaries where the α → β transformation starts. Diffusion mechanisms involving Al and Ti between the newly formed β and α' cannot be excluded at this stage. Hence, the combined effects of β phase formation at the plate boundaries and the variation of lattice parameters due to the diffusional processes are responsible of the modified mechanical behavior of the material after the firing cycle.

5. Conclusions

Acknowledgements

The research leading to these results has received funding from the European Union Seventh Framework Programme under grant agreement 312483 - Esteem2 (integrated infrastructure initiative–I3). The authors kindly acknowledge MSc. Adam Gruszczynski (AGH-UST) and A. Di Cristoforo (UNIVPM) for FIB lamellae and TEM sample preparation.

References

1. ImageJ
2. origin
3. Maud

G. Lutjering, J.C. Williams, "Titanium", Second Edition, Springer-Verlag, Berlin, 2007.

I.J. Polmear, “Light Alloys”, Fourth Edition, Elsevier Ltd, Oxford, 2006.

[D1] Ruben Wauthle, Bey Vrancken, Britt Beynaerts, Karl Jorissen, Jan Schrooten, Jean-Pierre Kruth, Jan Van Humbeeck, Effects of build orientation and heat treatment on the microstructure and mechanical properties of selective laser melted Ti6Al4V lattice structures, Additive Manufacturing 5 (2015) 77–84.

[D2] A.A. Antonysamy, J. Meyer, P.B. Prangnell, Effect of build geometry on the β-grain structure and texture in additive manufacture of Ti-6Al-4V by selective electron beam melting, Materials Characterization 84 (2013) 153-168.

[D3] Thijs L, Montero Sistiaga ML, Wauthle R, Xie Q, Kruth J-P, Van Hum-beeck J. Strong morphological and crystallographic texture and resulting yield strength anisotropy in selective laser melted tantalum. Acta Mater 2013;61:4657–68.

[D4] Thijs L, Verhaeghe F, Craeghs T, Humbeeck JV, Kruth J-P. A study of the microstructural evolution during selective laser melting of Ti–6Al–4V. Acta Mater 2010;58:3303–12.

[D5] Bey Vrancken, Lore Thijs, Jean-Pierre Kruth, Jan Van Humbeeck, Heat treatment of Ti6Al4V produced by Selective Laser Melting: Microstructure and mechanical properties, Journal of Alloys and Compounds 541 (2012) 177–185,

[D6] L.E. Murr, S.A. Quinones, S.M. Gaytan, M.I. Lopez, A. Rodela, E.Y. Martinez, D.H. Hernandez, E. Martinez, F. Medina, R.B. Wicker, Microstructure and mechanical behavior of Ti–6Al–4V produced by rapid-layer manufacturing, for biomedical applications, Journal of the Mechanical Behavior of Biomedical Materials 2 (2009) 20-32.

[D7] L.E. Murr, E.V. Esquivel, S.A. Quinones, S.M. Gaytan, M.I. Lopez, E.Y. Martinez, F. Medina, D.H. Hernandez, E. Martinez, J.L. Martinez, S.W. Stafford, D.K. Brown, T. Hoppe, W. Meyers, U. Lindhe, R.B. Wicker, Microstructures and mechanical properties of electron beam-rapid manufactured Ti–6Al–4V biomedical prototypes compared to wrought Ti–6Al–4V, Materials Characterization 60 (2009) 96-105.

[D8] Hiroaki Matsumoto, Hiroshi Yoneda, Kazuhisa Sato, Shingo Kurosu, Eric Maire, Damien Fabregue, Toyohiko J. Konno, Akihiko Chiba, Room-temperature ductility of Ti–6Al–4V alloy with α' martensite microstructure, Materials Science and Engineering A 528 (2011) 1512–1520

[D9] S. Leuders, M. Thöne, A. Riemer, T. Niendorf, T. Tröster, H.A. Richard, H.J. Maier, On the mechanical behaviour of titanium alloy TiAl6V4 manufactured by selective laser melting: Fatigue resistance and crack growth performance, International Journal of Fatigue 48 (2013) 300–307.

[D10] W. Xu, M. Brandt, S. Sun, J. Elambasseril, Q. Liu, K. Latham, K. Xia, M. Qian, Additive manufacturing of strong and ductile Ti–6Al–4V by selective laser melting via in situ martensite decomposition, Acta Materialia 85 (2015) 74–84.

[D11] M.M. Attallah, S. Zabeen, R.J. Cernik, M. Preuss, Comparative determination of the α/β phase fraction in α+β-titanium alloys using X-ray diffraction and electron microscopy, Materials Characterization 60 (2009) 1248-1256.

[D12] Hiroaki Matsumoto, Hiroshi Yoneda, Damien Fabregue, Eric Maire, Akihiko Chiba, Fumihiko Gejima, Mechanical behaviors of Ti–V–(Al, Sn) alloys with α' martensite microstructure, Journal of Alloys and Compounds 509 (2011) 2684-2692.

[D13] Hiroaki Matsumoto, Hiroshi Yoneda, Kazuhisa Sato, Shingo Kurosu, Eric Maire, Damien Fabregue, Toyohiko J. Konno, Akihiko Chiba, Room-temperature ductility of Ti–6Al–4V alloy with α' martensite microstructure, Materials Science and Engineering A 528 (2011) 1512–1520.

[D14] S.L. Semiatin, T.M. Brown, T.A. Goff, P.N. Fagin, D.R. Barker, R.E. Turner, J.M. Murry, J.D. Miller, F. Zhang, Diffusion coefficients for modeling the heat treatment of Ti–6Al–4V, Metall. Mater. Trans. A 35 (2004) 3015–3018.

[D15] Pere Barriobero-Vila, Guillermo Requena, Thomas Buslaps, Matthias Alfeld, Ulrike Boesenberg, Role of element partitioning on the α–β phase transformation kinetics of a bi-modal Ti–6Al–6V–2Sn alloy during continuous heating, Journal of Alloys and Compounds 626 (2015) 330–339.

[D16] J. W. Elmer, T. A. Palmer, S. S. Babu, W. Zhang, T. DebRoy, Phase transformation dynamics during welding of Ti–6Al–4V, J. Appl. Phys. 95, 8327 (2004).

[D17] J.W. Elmer, T.A. Palmer, S.S. Babu, E.D. Specht, In situ observations of lattice expansion and transformation rates of α and β phases in Ti–6Al–4V, Materials Science and Engineering A 391 (2005) 104–113.

[D18] J.W. Elmer, T.A. Palmer, S.S. Babu, E.D. Specht, Low temperature relaxation of residual stress in Ti–6Al–4V, Scripta Materialia 52 (2005) 1051–1056.

[D19] Akhilesh Kumar Swarnakar, Omer Van der Biest, Bernd Baufeld, Thermal expansion and lattice parameters of shaped metal deposited Ti–6Al–4V, Journal of Alloys and Compounds 509 (2011) 2723–2728.

[D20] R. Banerjee, P.C. Collins, D. Bhattacharyya, S. Banerjee, H.L. Fraser, Microstructural evolution in laser deposited compositionally graded α/β titanium-vanadium alloys, Acta Materialia 51 (2003) 3277–3292.